MS# 8119R1

Word count: about 6300

Crystal structure determination of orthorhombic variscite*2O* and its derivative $AlPO_4$ structure at high temperature

Matteo Ardit [a], Brian L. Phillips [b] and David L. Bish [c]

[a] Department of Physics and Earth Sciences, University of Ferrara, via Saragat 1, I-44122 Ferrara, Italy

[b] Department of Geosciences, Stony Brook University, Stony Brook, New York, NY 11794-2100, USA

[c] Department of Chemistry, Indiana University Molecular Structure Center, 800 E. Kirkwood Ave., Bloomington IN 47405-7102, USA

Authors e-mail: [a] rdtmtt@unife.it

[b] brian.phillips@stonybrook.edu

[c] bish@iu.edu

ABSTRACT

Variscite ($Al(PO_4)\cdot 2H_2O$) is an uncommon secondary phosphate mineral but is important in a variety of environmental and technological applications. It exists in at least one monoclinic (metavariscite) and two orthorhombic polymorphs ("Lucin-type" and "Messbach-type"), but the fine-grained nature of the "Messbach-type" variscite has hampered determination of its crystal structure. The crystal structure of the latter from Tooele County, Utah, was solved and refined using laboratory powder X-ray diffraction (XRD) data, charge-flipping, and the Rietveld method. Both variscite modifications belong to the family of framework 3D MT structures in which octahedra (M) and tetrahedra (T) are linked by bridging O atoms. Topological analysis reveals that the two structures are polytypes. Based on our results and our structural interpretations, we refer to "Lucin-

type" variscite as variscite*1O* and the "Messbach-type" as variscite*2O*, to be consistent with modern polytype terminology. The similarity of these two structures suggests that *1O*-*2O* interstratifications may exist in nature, which is consistent with observed broadening of diffraction peaks of the Tooele material. ^{31}P and ^{27}Al MAS/NMR measurements confirm the XRD-determined crystal structure and they show distinct signals for each of the two independent P and Al positions in variscite*2O*. High-temperature XRD, thermal analyses, and NMR measurements were applied to study the nature of the transformation of variscite*2O* to a derivative $AlPO_4$ structure above 473 K. Charge-flipping analysis showed that the crystal structure of the new anhydrous $AlPO_4$ phase ($AlPO_4$-var*2O* in analogy to its parent structure) can be described as a 3D framework of alternating AlO_4 and PO_4 tetrahedra linked by bridging O atoms. Thermogravimetric analyses revealed almost complete dehydration above ~450K, and NMR results were consistent with tetrahedral Al and P atoms.

Keywords: variscite; X-ray powder diffraction; charge-flipping; nuclear magnetic resonance; polytypism, $AlPO_4$.

INTRODUCTION

Interest in hydrated aluminophosphates and in compounds that derive from their dehydration spans a wide spectrum of disciplines. Variable crystal chemistry under ambient and non-ambient conditions, associated with interesting physical properties, makes this class of materials a subject of numerous studies. For example, variscite $Al(PO_4)\cdot 2H_2O$ (orthorhombic, s.g. *Pbca*; Kniep et al. 1977) and its monoclinic polymorph, metavariscite (s.g. $P2_1/n$; Kniep and Mootz 1973), as well as other hydrated aluminum phosphates are of great importance in environmental applications. Their dissociation helps regulate the release of phosphate in acidic soils (Lagno and Demopoulos 2005), their formation assists in purification of P-containing waste waters, and they have been employed to regulate the phosphate concentration in natural waters that, if too low, may hinder forest and

agricultural growth, but if too high, may lead to eutrophication (Oelkers and Valsami-Jones 2008). Technological applications at the industrial level mainly focus on the dehydrated forms of these minerals. In particular, it is well known that compounds with general formula $AlPO_4$ (molar Al/P ratio = 1) represent a polymorphic system closely related to that of silica. For instance, the mineral berlinite ($AlPO_4$) has the quartz crystal structure, and synthetic $AlPO_4$ compounds with the tridymite and cristobalite crystal structure are also known (Flörke 1967; Ng and Calvo 1976; Muraoka and Kihara 1977; Hensel et al. 2007). $AlPO_4$ compounds find application as molecular sieves (zeolite-type structures) and in heterogeneous catalysis (e.g., Wilson et al. 1982; Bordat et al. 2007), application in refractories (Pawlowski 1965), ceramics, and as insulating and protective surface coatings (Rothon 1981). From the petrologic and mineralogical point of view, sub-solidus phase relations in the ternary systems Al_2O_3-$AlPO_4$-H_2O (Wise and Loh 1976; Bass 1979) and Al_2O_3-P_2O_5-H_2O (Kniep 1986; Drüppel et al. 2007) have been studied at different temperatures and pressures to establish the stability fields and the origins of the known mineral species and to predict possible new species. Variscite and metavariscite are relatively rare secondary phosphate minerals (usually occurring with apatite, wavellite, and crandallite) that form at low temperatures as a result of the reaction of phosphate-bearing surface solutions with aluminum-rich rocks in near-surface environments (Larsen 1942). Their occurrence is summarized in Drüppel et al. (2007).

In addition to the metavariscite polymorph, variscite has two orthorhombic modifications, the so-called "Lucin-type" and the so-called "Messbach-type". Salvador and Fayos (1972) suggested that both of these have space group *Pbca* although the unit-cell volume reported for the "Messbach-type" is more than double that of the "Lucin-type". Salvador and Fayos (1972) argued that the "Lucin-type" cell may be considered as a "Messbach-type" pseudocell in which two independent AlO_6 and PO_4 polyhedra belonging to the asymmetric unit become equivalent. Unfortunately, it appears that complete structural data for the "Messbach-type" $AlPO_4 \cdot 2H_2O$ modification are lacking. As this modification always occurs in the form of cryptocrystalline aggregates (the occurrence of "Messbach-type" single crystals has been never reported in the literature), Salvador

and Fayos (1972) concluded that this variscite modification is a metastable crystalline state of orthorhombic aluminophosphates formed under natural conditions that do not facilitate development of long-range structural order.

In this work, the crystal structure of a natural specimen of the "Messbach-type" variscite from Tooele Co. (Utah, USA) was determined, and the dehydration process leading to the transition to a new $AlPO_4$ phase was monitored at high temperature. These phases were also examined by ^{31}P and ^{27}Al MAS/NMR spectroscopy, both of which confirmed the structure models. Based on our results and our structural interpretations, we hereafter refer to "Lucin-type" variscite as variscite*1O* and the "Messbach-type" as variscite*2O*, to be consistent with modern polytype terminology (e.g., Guinier et al. 1984).

EXPERIMENTAL

Specimen description

All experiments in the present study were performed on a pale green cryptocrystalline variscite specimen from Tooele County (Utah, USA). The specimen, which belongs to the mineralogical collection of the Department of Earth and Atmospheric Sciences at Indiana University (collection code T-1793), occurs with metavariscite, quartz, and crandallite as the primary associated phases. Prior to analysis, visually pure portions of the specimen were extracted and ground under acetone in an agate mortar and pestle. We assumed the ideal chemical composition, similar to the chemistry reported by Calas et al. (2005) for variscite from Utah. In addition, a semiquantitave chemical analysis of the investigated specimen was reported as supplemental material (experimental procedure and chemical analysis in Table S1).

X-ray powder diffraction

X-ray powder diffraction data were collected both at room- and high-temperature (RT and HT) conditions. *Experimental setup 1* - RT data collection was performed on a Bruker D8 Advance diffractometer equipped with a SolX Si(Li) solid-state detector set to discriminate Cu $K\alpha_{1,2}$ radiation. The variscite powder was loaded in a 1 mm-deep cavity in a Ti holder and scanned in continuous mode from 2-140° 2θ, with step size of 0.02° 2θ and a counting time of 23 s per step. *Experimental setup 2* - the same powder was placed in a cavity specimen holder on an Anton-Paar TTK 450 temperature stage. HT data were collected on a Bruker D8 Advance diffractometer equipped with a VÅNTEC-1 detector operating in scanning mode in the 12-80° 2θ angular range, with an effective step size of 0.017° 2θ and a counting time of 1 s per step. XRD patterns were recorded every 50 K from RT to 723 K in air with a heating rate of 10 $K \cdot min^{-1}$. In combination with parallel thermogravimetric - differential thermal analysis (TG-DTA) data, the HT powder diffraction experiment was formulated to provide a continuous picture of the structural response to dehydration. An additional measurement at RT (using experimental setup 1) was performed on the HT sample after heating.

Thermogravimetric analysis

TG-DTA measurements used a TA Instruments SDT 2960 v3.0F device. An aliquot of the ground sample (20.32 mg) was placed in an alumina crucible and heated from 297 to 865 K at a rate of 10 $K\ min^{-1}$ under a static (non-flowing) air atmosphere.

NMR Spectroscopy

^{31}P and ^{27}Al MAS/NMR spectra were acquired at 202.2 and 130.23 MHz, respectively, with a 500 MHz (11.7 T) Varian Infinityplus spectrometer and Chemagnetics-type probe assembly configured for 3.2 mm (o.d.) rotors. The acquisition parameters for the ^{31}P experiments include 12 kHz spinning rate and 5 μs 90° pulses separated by 10 s relaxation delays, yielding fully relaxed spectra. The ^{27}Al spectra were taken at a spinning rate of 18 kHz with 1 s relaxation delays between 0.5 μs

This is the peer-reviewed, final accepted version for American Mineralogist, published by the Mineralogical Society of America.
The published version is subject to change. Cite as Authors (Year) Title. American Mineralogist, in press.
DOI: https://doi.org/10.2138/am-2022-8119. http://www.minsocam.org/

pulses of a transverse RF field corresponding to a 4.5 μs non-selective 90° pulse (56 kHz). Several ^{27}Al-observed, ^{31}P-dephased rotational echo double resonance (REDOR) data sets were also acquired to investigate the nature of minor peaks. These experiments employed a Chemagnetics-style triple resonance probe based on a 4 mm spinning assembly and a 12.5 kHz sample spinning rate. The ^{27}Al spin-echo spectra were obtained with selective 90°/180° pulses of 8 and 16 μs. ^{31}P-dephasing was achieved by applying 10μs ^{31}P 180° pulses every one-half rotor period. A 5.1 ms dephasing time was sufficient to eliminate signal from the major aluminum phosphate phases. A 400 MHz Varian Inova spectrometer was used to acquire two-dimensional ^{27}Al MQ-MAS spectra at a 20 kHz spinning rate. The excitation and conversion pulses were 2.5 and 1.1 μs, respectively, followed by a 15 μs selective 90° pulse which was phase cycled to select the triple-quantum/single-quantum coherence. Data collection for the indirect (F_1, isotropic) dimension used 192 scans for 100 steps incremented by 50 μs, giving a 20 kHz spectral window in F_1 that is equal to that used to acquire the direct, anisotropic F_2 dimension. Chemical shifts were measured against external 85% H_3PO4 (^{31}P) and acidified 0.1*m* $Al(NO_3)_3$ solutions.

STRUCTURE SOLUTION AND REFINEMENT

Qualitative phase analysis was performed using the Bruker AXS EVA software (v.5) on the powder diffraction data collected at RT. In addition to the presence of metavariscite, crandallite, and quartz, an almost perfect match of the diffraction peaks was provided by variscite in its *2O* modification as indexed by Salvador and Fayos (1972). No calculated diffraction patterns were available for this aluminophosphate, as no crystal structure models for variscite*2O* are reported in the literature.

Indexing and whole-powder-pattern decomposition (WPPD)

Preliminary least-squares indexing of the powder diffraction pattern measured at RT was performed using the single-value decomposition method (Coelho 2003) as implemented in TOPAS v. 5.0. Indexing of the RT data for the variscite sample was performed using 58 diffraction peaks below 50° 2θ, avoiding those peaks belonging to associated phases. Among the possible solutions, that with the best goodness of fit corresponded to space group *Pbca* (No. 61). A subsequent WPPD was performed with a Pawley profile fit (Pawley 1981), and the resulting unit-cell parameters were: a = 9.9008(12) Å, b = 17.1915(17) Å, c = 9.6670(14) Å, V = 1645.4(3) Å^3 with an R_{wp} of 0.052. The Pawley profile fit returned the least-squares minimization A-matrix (Marquardt 1963) containing the reflection indices and intensities for subsequent structural determination through the charge-flipping algorithm (CFA).

Charge-flipping structure solution

Ab initio crystal structure solution of variscite*2O* at RT was performed using the CFA (Oszlányi and Sütő 2004; Coelho 2007; Palatinus 2013). Along with the A-matrix, unit-cell parameters obtained from Pawley fitting were used as input data. In order to sharpen electron density clouds, all reflections were included in the CFA, extending the Ewald sphere to 0.82 Å (~140° 2θ with Cu radiation). Furthermore, the CFA was constrained to maintain the symmetry found during the WPPD (i.e., orthorhombic *Pbca*). Other macros were used to avoid electron density perturbations and to increase the number of grid points.

A structure solution (R factor of 0.57) was found after 99 iterations. The number of merged reflections was 1681 (834 of them "weak"). ~~The resulting graphical output of the CFA structure determination (Fig. 1) highlights the presence of alternating octahedrally coordinated Al atoms that share corners with tetrahedrally coordinated P atoms.~~

Rietveld refinement

The structure model of variscite*2O* obtained through the CFA was refined using the fundamental-parameter (FP) Rietveld approach (TOPAS v.5.0) (Cheary and Coelho, 1992; Cheary et al., 2004; Rietveld, 1967; Rietveld, 1969). Associated metavariscite, crandallite, and quartz (starting structure models from Kniep and Mootz (1973), Blount (1974), and Gualtieri (2000), respectively) were modeled by carrying out multiphase refinements in which only the scale factors and unit-cell parameters for these three phases were varied. Known instrumental parameters (e.g., goniometer radius, slit sizes, geometrical parameters of the X-ray tube, etc.) were used to calculate the instrumental contribution to the peak profiles, and specimen-related Lorentzian crystallite size and strain broadening information for each phase was extracted from the observed profiles. An instrumental zero error was fixed at the value determined using a NIST LaB_6 standard, and refinement included a specimen displacement correction and a five-term Chebyshev polynomial (along with a 1/X coefficient to model the low-angle background) to model the background. Unit-cell parameters, atomic coordinates, and isotropic atomic displacement parameters ADPs (B_{iso}) were varied for variscite*2O*. During refinement of the atomic coordinates a set of soft constraints with a tolerance of 0.03 Å was applied to the P–O (1.54 Å) and Al–O (1.91 Å) bond distances. When the calculated standard deviation of the bond lengths was smaller than the tolerance applied to the constrained bond distances, the weight applied to the soft constraints, imposed as additional observations at the earlier stages of the refinement, was progressively lowered until atomic coordinates were allowed to vary almost freely. ADPs for a given atom type (i.e., Al, P, and O) were constrained to be equivalent. The Rietveld refinement plot of the variscite sample data collected at RT is shown in Fig. 1, and agreement factors and unit-cell parameters are summarized in Table 1. Metal-oxygen bond distances and bond angles for the variscite*2O* crystal structure are reported in Table 2. Final atomic coordinates and ADPs for the variscite*2O* crystal structure (Table S2) and a crystallographic information file have been deposited as electronic supplemental material.

XRD pattern evolution at HT

The evolution of the XRD patterns for the variscite sample (for sake of clarity over the 13–38° 2θ angular range) from room temperature to 723 K is shown in Fig. 2*a*. Qualitatively, the patterns collected at RT and 323 K were virtually identical. At temperatures > 323 K, all peaks broadened (except for those of quartz, which changed little up to the maximum investigated temperature), and peaks belonging to metavariscite and crandallite were undetectable. At temperatures > 473 K, the characteristic peaks of variscite*2O* disappeared, and the occurrence of a phase whose powder diffraction pattern resembled that of an $AlPO_4 \cdot nH_2O$ phase previously reported by d'Yvoire (1961; ICDD reference code: 00-015-0246) is recorded. With reference to the TGA/DTA data discussed below, *n* was close to 0 mol for this material.

Indexing, WPPD, structure solution, and Rietveld refinement of the new $AlPO_4$-var*2O* structure

In order to identify the symmetry, space group, and unit-cell parameters of the new high-temperature phase, least-squares indexing of the XRD pattern collected at RT after heating to 723 K was performed using the single-value decomposition method (Coelho 2003). With the exception of those peaks belonging to quartz, the first 20 diffraction peaks below 50° 2θ were indexed. Among the possible solutions, a very good match was obtained by indexing the pattern in the orthorhombic crystal system with space group *Pbca* (No. 61). Subsequent WPPD with a Pawley profile fit (Pawley 1981) confirmed this space group, and the resulting unit-cell parameters were: a = 9.969(3), Å b =17.145(4) Å, c = 8.636(2) Å, V = 1476.2(6) Å^3 with an R_{wp} of 0.09. As previously described for variscite*2O*, *ab initio* crystal structure solution of the new $AlPO_4$ phase was performed using the CFA. Due to the partial loss of structural order as a function of temperature, which broadened the measured diffraction peaks, only the positions of some of the sharpest electron density clouds were identified. This partial solution, however, was sufficient for full structure solution and validation by a three-dimensional (3D) Fourier analysis. Unlike the variscite*2O* parent structure, the crystal structure of this new $AlPO_4$ phase (hereafter $AlPO_4$-var*2O* in analogy to its

parent structure) can be described as a 3D framework of alternating AlO_4 and PO_4 tetrahedra linked by bridging O atoms (Fig. 3).

This structure model was subsequently refined using a FP Rietveld approach, following the same procedure described above for the variscite*2O* crystal structure. The Rietveld refinement plot of the variscite sample collected at RT after heating at 723 K is shown in Fig. 4, and agreement factors and unit-cell parameters are summarized in Table 3. Metal-oxygen bond distances and bond angles for the $AlPO_4$-var*2O* crystal structure are reported in Table 4. Final atomic coordinates and ADPs for the $AlPO_4$-var*2O* crystal structure (Table S3) and a crystallographic information file have been deposited as electronic supplemental material.

RESULTS AND DISCUSSION

Thermal analysis

TG–DTA curves for the variscite sample are shown in Fig. 5. These data closely resemble those for other phases with composition $AlPO_4 \cdot 2H_2O$ (i.e., variscite*1O* and metavariscite) (Boonchom and Danvirutai 2009; Prado-Herrero et al. 2010). The TG-DTA curves reveal multiple decomposition steps at temperatures below 473 K. Specifically, TG analysis showed a small, continuous weight loss (1.6 wt.%) up to ~373 K, likely due to the release of adsorbed H_2O, and from ~373 K to 473 K a significant weight loss of 20.4 wt% occurred. A small, gradual weight loss was detected at higher temperatures. The DTA curve displays two poorly resolved small endotherms below 373 K, above which the data reveal the beginning of variscite*2O* decomposition and the phase transition into a dehydrated phase. This transition is reflected by a large endotherm between 373 and 473 K and centered at ~425 K, resulting from the loss of H_2O molecules associated with the Al octahedra. It is worth noting that the large endotherm centered at ~425 K in the DTA curve corresponds to a weight

loss equal to one molecule of H_2O for each unit of $AlPO_4$ $2H_2O$. The retained mass of ~77% is compatible with the value expected for the formation of a phase with $AlPO_4$ composition.

NMR spectroscopy

The ^{31}P and ^{27}Al MAS/NMR spectra of variscite*2O* and the dehydrated $AlPO_4$-var*2O* are displayed in Fig. 6. These spectra show distinct signals for each of the two independent P and Al positions in variscite*2O* and a change in Al coordination after heating at 523 K to form $AlPO_4$-var*2O*. The ^{31}P NMR spectrum of variscite*2O* (Fig. 6a) contains narrow peaks at -17.0 and -20.3 ppm, with FWHM values of 0.8 and 0.9 ppm, respectively. The fitted integral ratio, 1:1.06(5), is consistent with assignment to the distinct P positions of variscite*2O*. These chemical shifts are similar to those reported previously for variscite and metavariscite (Blackwell and Patton 1984; Bleam et al. 1989). The spectrum also contains several additional signals, including a broad peak centered near -5.4 ppm (6 ppm FWHM), a position similar to the chemical shift for crandallite reported by Bleam et al. (1989), a small peak near -8.4 ppm that cannot be assigned based on previous work, and a shoulder near -19 ppm that likely arises from metavariscite (Blackwell and Patton, 1984). After heating at 523 K, a broader peak at -28.7 ppm, 2.8 ppm FWHM, dominates the ^{31}P spectrum (Fig. 6b), although the smaller peak near -5.4 ppm remains. The increased width of the peak for $AlPO_4$-var*2O* indicates a loss of structural order with heat treatment and parallels the increased width observed in the diffraction peaks.

The centerband of the ^{27}Al MAS/NMR spectrum of variscite*2O* at 11.7 T (Fig. 6c) is dominated by a feature spanning the range -10 to -20 ppm that displays fine structure from second-order quadrupolar effects, in addition to a smaller peak centered near 0 ppm. The origin of this minor peak is unclear as its apparent chemical shift is inconsistent with octahedral or tetrahedral Al in an aluminophosphate. The retention of this minor peak in fully ^{31}P-dephased $^{27}Al/^{31}P$ REDOR spectra suggests the corresponding Al atoms are not associated with phosphate. The main centerband peak is accompanied by a wide manifold of narrow spinning sidebands (SSB's) arising from the

±(3/2,1/2) satellite transitions that spans over ±500 kHz and clearly resolves two distinct sets. The positions of the ±1, ±2, and ±3 satellite SSB's, which occur at frequencies offset from the centerband by ±*n* multiples of the spinning rate, were averaged to obtain centers of gravity for the satellite transitions, -5.8 and -8.9 ppm. The innermost (*n* = 1 and *n* = -1) satellite SSB's are shown as insets in Fig. 6c. The reduced contribution of the second-order quadrupolar broadening to the width of the satellite SSB's compared with the centerband (Samoson 1985) allows resolution of the signal from the two Al positions of variscite*2O*. Two distinct resonances are also observed in the two-dimensional MQ-MAS spectrum taken at 9.4 T (Fig. 7), showing clearly resolved peaks in the isotropic (*F*1) dimension at -6.8 and -1.8 ppm. Alignment of the positions of the spectral features observed in the corresponding anisotropic (*F*2) cross-sections (Fig. 7, right panel) with those of calculated second-order quadrupolar MAS lineshapes yields the quadrupolar coupling constants C_q = 2.7 and 3.5 MHz and asymmetry parameters η = 0.5(1) and 0.95(5) ppm for the two signals (Table 5). The quadrupolar shifts of the ±(3/2,1/2) satellite transitions were calculated from these quadrupolar coupling parameters and added to the SSB centers of gravity to arrive at the corresponding isotropic chemical shifts (Table 5).

A large shift of the main ^{27}Al NMR centerband occurs after heating at 523 K to form $AlPO_4$-var*2O*, from ca. -15 to +39 ppm (cf. Fig. 6c,d). The latter value is consistent with four-coordinated Al in tetrahedral aluminophosphate frameworks (Blackwell and Patton, 1983; Müller et al. 1984) and with the loss of the two coordinating H_2O molecules bonded to the $AlO_4(OH_2)_2$ octahedra in variscite*2O*. This spectrum also contains a small peak centered near +5 ppm that appears somewhat narrower than for the unheated sample, but it is similarly retained in REDOR ^{31}P dephasing experiments. The main centerband peak is accompanied by a wide manifold of narrow ±(3/2,1/2) satellite SSB's extending ±385 kHz from the centerband, from which it was possible to estimate a C_q value of 2.0(2) MHz (Table 5). The isotropic chemical shift, δ_{iso} = +40.2(2) ppm, was determined from the center of gravity of the ±(3/2,1/2) satellite transition SSB's by correcting for

the quadrupolar shift. This value also agrees with the difference in the centerband peak position observed at 9.4 vs. 11.7 T. Presenting featureless and nearly symmetric peak shapes, the centerband and satellite SSB's at 11.7 and 9.4 T show no evidence of second-order quadrupolar features or resolution of the distinct Al sites of $AlPO_4$-var*2O*. Likewise, a two-dimensional MQ-MAS spectrum taken at 9.4 T (not shown) contains only a single peak with a symmetrical profile in both the isotropic and anisotropic dimensions.

Owing to the interest in microporous aluminophosphates for chemical applications, a large number of such materials have been characterized by XRD and NMR spectroscopy, from which relationships between structure and spectroscopic parameters are available to aid assignment of the resonances observed here. Kanehashi et al. (2007) and Dawson et al. (2017), building on the earlier observations of Müller et al. (1984), developed correlations of ^{31}P NMR chemical shifts with structural parameters that depend mainly on the average P–O–Al angle and also on the average P–O distance in the case of Eqn. 2 of Dawson et al. (2017). The ^{31}P chemical shifts calculated from the three expressions and the variscite*2O* crystal structure data of the present study range from -20.1 to -20.3 for P1 and from -18.6 to -18.2 ppm for P2. These chemical shift correlations suggest assignment of the peak at -20.3 ppm to P1 and that at -17.0 ppm to P2 (Table 5). These assignments conform to the general relationship observed for tetrahedral cations of more negative chemical shifts for larger average T–O–M interpolyhedral angles (Müller et al. 1984), although such expressions have been derived mainly from data for tetrahedral framework structures. Similar calculations for the phosphate tetrahedra of $AlPO_4$-var*2O* yield overlapping chemical shift ranges for P1 and P2 (Table 5). The average P–O–Al angle for the $P1O_4$ and $P2O_4$ tetrahedra differ by only 0.2°, which suggests a difference in chemical shift of 0.2-0.3 ppm for $AlPO_4$-var*2O*. This peak separation is far less than the half-width of the peaks observed for variscite*2O*, preventing resolution of signals for P1 and P2 in the ^{31}P MAS/NMR spectrum. We note further that application of low-power ^{27}Al-decoupling during acquisition (e.g., Delevoye et al. 2002) had no significant effect on the ^{31}P NMR spectra of either sample.

Although no ^{27}Al chemical shift correlation similar to that for ^{31}P has been proposed for octahedral Al, a linear relationship with a slope of ca. -0.5 ppm/degree has been noted for tetrahedral Al in condensed aluminophosphates (Müller et al. 1984) and for aluminosilicates (Lippmaa et al. 1986). The tetrahedral-octahedral framework topology of variscite*2O* and the similar coordination environment of the two Al positions suggest that differences in chemical shift could reflect variation in average Al–O–P angle. Assumption of such a relationship leads to the tentative assignment of the resonance exhibiting a more negative chemical shift to Al1, which has the larger average Al–O–P angle, 140.9°, compared with 137.8° for Al2. Relationships have previously been proposed between the quadrupolar coupling constant (C_q) for octahedral Al and the longitudinal strain and shear strain of the coordination polyhedron (Ghose and Tsang, 1973), although it is recognized that the electric field gradient at the nucleus might reflect structural factors at longer distances. The $Al2O_4(OH_2)_2$ octahedron appears more distorted than that of Al1 in terms of both longitudinal (0.040 vs. 0.037) and shear (0.63 vs. 0.49) strain, parallel to the trend in octahedral quadratic elongation and angle variance (Table 2). This observation suggests assignment of the resonance exhibiting the larger C_q value to the more distorted $Al2O_4(OH_2)_2$ octahedron. Consideration of differences in average interpolyhedral Al–O–P angle leads to the same assignment scheme, with the resonance exhibiting more negative chemical shift and smaller C_q value (Table 5) corresponding to Al1 (larger Al–O–P angle, less distorted coordination polyhedron).

The ^{27}Al MAS/NMR data for $AlPO_4$-var*2O* show single, nearly symmetrical peaks for both the centerband and the ±(3/2,1/2) satellite SSB's, whereas the crystal structure contains two distinct Al positions. The correlation given by Müller et al. (1984) suggests a chemical shift separation of ca. 1.8 ppm between Al1 and Al2, from the 3.6° difference in average Al–O–P angle for the $Al1O_4$ and $Al2O_4$ tetrahedra. A second-order quadrupolar MAS lineshape for the C_q of 2 MHz determined for $AlPO_4$-var*2O* exhibits a FWHM of about 2.2 ppm under the conditions of the present study. Addition of two such calculated MAS peak shapes, separated by the 1.8 ppm estimated chemical shift difference between Al1 and Al2, yields an unresolved composite peak with a width of 3.6

ppm, similar to the 4.0 ppm observed value. Englehardt and Veeman (1993) proposed a linear correlation between C_q and the tetrahedral shear strain of Ghose and Tsang (1974) for tetrahedral Al in aluminophosphates, from which we estimate C_q values of 2.5 and 2.3 MHz for Al1 and Al2, respectively. These values are similar to but somewhat larger than we observe. The difference in isotropic (*F*1) MQ-MAS peak positions for Al1 and Al2 calculated from the estimated C_q values and chemical shift difference is 2.1 ppm at 9.4 T. This separation is significantly smaller than the observed MQ-MAS F1 peak width, 4.2 ppm FWHM. These observations suggest that similar C_q values and a chemical shift difference smaller than the inherent linewidth prevents resolution of Al1 and Al2 in our ^{27}Al MAS-NMR spectra of $AlPO_4$-var*2O*.

Crystal structure description of variscite*2O* and comparison with variscite*1O*

Like variscite*1O*, the variscite*2O* crystal structure belongs to the family of framework 3D MT structures in which octahedra (M) and tetrahedra (T) are linked by bridging O atoms (Ilyushin and Blatov 2017). The structure contains independent Al^{3+} cations coordinated by two H_2O molecules and four oxygen atoms of phosphate groups. Independent PO_4 tetrahedra share their corners with four adjacent $AlO_4(OH_2)_2$ octahedra (Fig. 8).

Both structures crystallize in the orthorhombic system (s.g. *Pbca*) and all atoms are in the general position (8*c* Wyckoff position). The mean tetrahedral bond lengths for both variscite structures are equivalent (within uncertainties), whereas the mean octahedral bond lengths for variscite*2O* are slightly longer than for variscite *1O* (i.e., 1.913(6) and 1.919(6) Å for variscite*2O* versus 1.897(2) Å for variscite*1O* (Kniep et al. 1977), respectively). Analysis of the IR spectra for both variscite modifications reported by Salvador and Fayos (1972) suggested the presence of two types of H_2O molecules (*i.e.*, *W*1 and *W*2). Based on the relative intensity of the associated IR bands, the latter authors argued that the *W*1:*W*2 proportion was 1:1 versus 3:1 for variscite*1O* and variscite*2O*, respectively. Although the fine-grained nature of the variscite specimen investigated here prevented the possible location of hydrogen atoms (a neutron diffraction experiment at a large-scale facility,

which is beyond the scope of the present study, is required), the comparison of the refined Al–O_W bond distances for the two variscite structures suggests that the H_2O molecule proportion reported by Salvador & Fayos (1972) is correct. In fact, the mean Al–O_W bond distance for variscite*1O* is 1.937(7) (Kniep et al., 1977), and that of Al1–O_W and Al2–O_W for variscite*2O* are 1.923(6) and 1.936(6) Å, respectively. Although the Al1–O_W distance of variscite*2O* perfectly matches that of the *1O* modification, the longer ⟨Al2–O_W⟩ bond could be related to the different H_2O molecule proportion reported by Salvador & Fayos (1972).

At first glance, comparison of unit-cell parameters for variscite*1O* (Kniep et al. 1977) and *2O* reveals that the unit-cell of the *2O* modification is very similar to that of *1O* except for a doubling of the *b*-axis (17.18 vs 8.56 Å for *2O* and *1O*, respectively). In fact, variscite*2O* is characterized by larger unit-cell parameters that lead to a doubling of the unit-cell volume plus a volume excess of about 1.4 % (i.e., $V_{\text{variscite}2O} \approx 2 \cdot V_{\text{variscite}1O} + 1.4\%$). Salvador and Fayos (1972) suggested that the unit-cell of variscite*1O* can be considered as a pseudocell of the variscite*2O* in which independent polyhedra (i.e., $P1O_4$ and $P2O_4$ tetrahedra and $Al1O_4(OH_2)_2$ and $Al2O_4(OH_2)_2$ octahedra, respectively) belonging to the asymmetric unit become equivalent.

As often reported in the case of framework structures, a cell-pseudocell relationship as hypothesized by Salvador and Fayos (1972) for *1O* and *2O* variscite structural modifications could entail an isosymmetric phase transition. However, this kind of situation is not plausible as a much smaller volume variation should be involved (e.g., Angel 1996).

As shown in previous work on aluminophosphate hydrates (e.g., Ilyushin and Blatov 2017; Kolitsch et al. 2020), evidence of a possible relationship among different crystal structures can be inferred by inspecting their topology. Although the variscite structure is based on a 3D MT framework, only four vertices of each $AlO_4(OH_2)_2$ octahedron are bridging, whereas the remaining vertices are H_2O molecules that do not participate in framework formation (Fig. 8). Hence, the variscite topology can be viewed as a 4-connected 3D framework yielding a series of hexagonal two-dimensional (2D) nets linked in the direction perpendicular to the net plane (Kolitsch et al. 2020). Based on the

enumeration of 3D networks from hexagonal nets provided by Smith (1977), the topological features of variscite*1O* and *2O* are shown in Fig. 9.

This graphical approach symbolically represents both tetrahedral and octahedral polyhedra as nodes, with black and white nodes pointing upward and downward, respectively. Two adjacent nodes of a horizontal hexagon can have additional linkages pointing in either the same (**S**) or changed direction (**C**), meaning that each edge of the net is associated with either the **S** or **C** symbol (Smith 1977).

As previously reported for isomorphic compounds (Kolitsch et al. 2020), the variscite*1O* 2D net is based on hexagons with the **SCSCCC** cyclic symbol (Fig. 9a and b). In contrast, hexagons that compose the 2D net in variscite*2O* are characterized by two cyclic symbols **SCSCCC** and **SCCSCC** (Fig. 9c and d). As highlighted by Smith (1977), the occurrence of more than one type of cyclic sequence is quite uncommon. He reported that only one framework type with alternating **CCCCCC** and **SCSCCC** hexagons has been found in 2D hexagonal nets, i.e., for the beryllonite and trimerite crystal structures (Smith, 1977 and references therein).

As with the structural modifications of variscite*1O* and *2O*, the topology of metavariscite is also based on a 6.6.6 2D net. Hexagons describing the metavariscite topological motif consist only of the **SCCSCC** cyclic symbol (Bennet et al 1986; Kolitsch et al. 2020). Although based on a common 2D net topology, variscite*1O* and metavariscite do not display a polytypic relationship (Bennet et al. 1986) and they are polymorphs (e.g., Taxer and Bartl 2004; Ilyushin and Blatov 2017; Kolitsch et al. 2020).

A further way to inspect the topological features of the *1O* and *2O* variscite modifications can be achieved through representation of the same 2D sheets of hexagons by representing tetrahedral and octahedral polyhedra as black and white apices, respectively, thereby emphasizing the heteropolyhedral arrangement of these aluminophosphates (Krivovichev 2007). In addition to this type of symbolism, different stacks of hexagons generated by the same polyhedral clusters (i.e., by the same atomic arrangement) have been highlighted with different colors in Fig. 10.

Differences in the periodicity of stacking hexagonal sequences, where ABAB... and AA'BB'... motifs have been identified for the *1O* and *2O* variscite structural modifications, respectively, are highlighted in Fig. 10 (*a* and *b*). Topological analysis of variscite*1O* and *2O* suggests that these structures can be considered polytypes. ~~The linkage of the 2D nets of hexagons for both variscite modifications results in the formation of four-membered rings perpendicular to the 2D nets, whose idealized topology has been represented in Fig. 10 (*b* and *d*).~~ Figure 11 clearly shows that the topology of variscite*1O*, which is the basis of the monoclinic $CaGa_2O_4$ framework (Smith 1977; Kolitsch et al. 2020), is exclusively based on boat-shaped 6-membered rings (MR) whereas that of variscite*2O* can be described as boat-shaped eight-membered rings (MR) connected via 4-MR to boat-shaped 6-MR (Fig. 11).

The polytypic relationship between variscite*1O* and *2O* suggests the possibility of structural disorder in variscite. A situation similar to the disorder occurring in opal-CT (e.g., Guthrie et al. 1995) can be envisioned, wherein an interstratified *1O* and *2O* structure is formed. This interstratification would give rise to broadening of diffraction peaks and formation of two-dimensional diffraction features and other non-Bragg scattering features (these features may be responsible for deviations between observed and calculated peak intensities in the Rietveld refinement pattern shown in Fig. 1 in the 13–35° 2θ angular range). Such interstratification is distinct from a physical mixture of discrete variscite*1O* and *2O* crystallites, and this structural disorder should be observable in high-resolution transmission electron microscope images.

Evolution of the $AlPO_4$-var*2O* unit cell with temperature; comparison with the parent structure variscite*2O*

The temperature dependence of the unit-cell volume and normalized unit-cell parameters for the $AlPO_4$-var*2O* phase are reported in Fig. 12. Over the investigated temperature range, the unit-cell volume as well as the unit-cell parameters of the dehydrated aluminophosphate vary continuously and smoothly with temperature, and no evidence of a first-order phase transition was observed (Fig.

12). In addition, Fig. 12b shows that $AlPO_4$-var*2O* is characterized by a strong anisotropic axial expansion, wherein the *a* axis expands more rapidly than the *b* axis and the *c* axis is almost unaffected over this temperature range.

Comparison of the polyhedral angle variance (AV) for variscite*2O* and $AlPO_4$-var*2O* crystal structures (Tables 2 and 4) reveals that the structure of the high-temperature phase is overall more distorted. With the exception of the $P1O_4$ tetrahedron, where a slight decrease of TAV was observed, both Al polyhedra and the $P2O_4$ tetrahedron experience a remarkable increase in AV in the $AlPO_4$-var*2O* structure. The intrapolyhedral AV departure from ideal values (OAV and TAV are 0 for ideal bond angles in regular octahedra and tetrahedra, respectively; Robinson et al. 1971) are partially compensated by interpolyhedral bond angles (*M*–O–*T* and *T*–O–*T*, for variscite*2O* and $AlPO_4$-var*2O*, respectively) that become more obtuse at high temperature (Tables 2 and 4). An irrefutable indication of the increased lattice distortion for the $AlPO_4$-var*2O* structure is provided by the calculation of the bond valence (*BV*, Hawthorne 2015; Brown 2016) for Al and P polyhedra (Table 6). Although the polyhedral BV_{sum} for variscite*2O* almost perfectly matches the formal charges of cations at each polyhedral site (only the $Al2O_4(OH_2)_2$ octahedron is slightly underbonded), the polyhedral BV_{sum} for $AlPO_4$-var*2O* is far from the cations' formal charges. Specifically, AlO_4 tetrahedra are strongly overbonded and the $P2O_4$ tetrahedron is slightly underbonded. The Pauling bond-strength sums at each Al coordinated to O exceed by ~15% on average that of an ideal bonded O with Al in tetrahedral coordination (i.e., 0.75 v.u.).

IMPLICATIONS

These results demonstrate for the first time that polytypism is an inherent property of variscite. The polytypic nature of variscite structures, which is related to different atomic stacking sequences along the *b*-axis, suggests the possible occurrence of interstratified hydrated Al-phosphate structures. Distinct from a physical mixture of discrete variscite*1O* and *2O* crystallites,

interstratified *1O* and *2O* structures would lead to structural disorder analogous to that observed in opal-CT (Guthrie et al. 1995), vaterite (Makovicky 2016), and many other polytypic structures in minerals (e.g., Zvyagin 1988; Baronnet 1992; and literature therein). Variscite structures have almost the same density (i.e., 2.59 and 2.49 $g \cdot cm^{-3}$ for polytype *1O* and *2O*, respectively) and, on the basis of interaction models to described the energetics of polytypic structures (e.g., Smith et al. 1984, Price and Yeomans 1984; Angel et al. 1985; Angel 1986), will have the same or very similar Gibbs free energy.

Our new data enhance the understanding of polytypism and polymorphism in this system. In addition, our results demonstrate that topological analysis proves to be an effective tool in identifying the polytypic nature of crystal structures.

The present results also demonstrate that dehydration of variscite can occur without altering the framework topology. The relatively low temperature at which dehydration begins suggests the possibility of the occurrence in nature of $AlPO_4$-var*2O* or material with an intermediate hydration state, depending on the ease of rehydration. The Al-coordination change from octahedral to tetrahedral that accompanies dehydration, clearly demonstrated by the ^{27}Al NMR data, confirms the removal of the Al-bound H_2O molecules as the dehydration mechanism, transforming the variscite octahedral-tetrahedral framework to a purely tetrahedral framework. The large separation and narrow widths of the ^{27}Al NMR peaks for octahedral and tetrahedral Al observed in the present study indicate that the variscite hydration state can be assessed simply from the intensity ratio of these peaks. Whether intermediate states of hydration result in pentacoordinated Al remains to be investigated, but such species should yield a distinct NMR signal. There are many examples in the literature of reversible conversion of aluminophosphates by hydration/dehydration between purely tetrahedral frameworks and those containing both tetrahedral and octahedral Al, but variscite appears thus far unique in such a relationship involving a strictly alternating tetrahedral-octahedral framework containing only octahedral Al.

Acknowledgments

We thank Laura Chelazzi (CRIST - Centro di Servizi di Cristallografia Strutturale, University of Firenze) for XRF analysis. We thank Christian L. Lengauer and an anonymous reviewer for constructive reviews.

Funding

MA acknowledges financial support by the grant from the Italian Ministry of Education (MIUR) through the project "Dipartimenti di Eccellenza 2018–2022".

References

Angel, R.J., Price, G.D., and Yeomans, J. (1985) Energetics of polytypic systems: Further applications of the ANNNI model. Acta Crystallographica B, 40, 310-318.

Angel, R.J. (1986) Polytypes and polytypism. Zeitschrift für Kristallographie, 176, 193-204.

Angel, R.J. (1996) New phenomena in minerals at high pressures. Phase Transitions, 59, 105-119.

Baronnet, A. (1992) Polytypism and stacking disorder. In P.R. Buseck, ed., Minerals and Reactions at the Atomic Scale: Transmission Electron Microscopy, 27, 231-288. Reviews in Mineralogy and Geochemistry, Mineralogical Society of America, Chantilly, Virginia.

Bass, J.D. (1979) The stability of trolleite and the Al_2O_3-$AlPO_4$-H_2O phase diagram. American Mineralogist, 64, 1175-1183.

Bennett, J.M., Dytrych, W.J., Pluth, J.J., Richardson Jr, J.W., and Smith, J.V. (1986) Structural features of aluminophosphate materials with Al/P = 1. Zeolites, 6, 349-360.

Blackwell, C.S., and Patton, R.L. (1984) Aluminum-27 and phosphorus-31 nuclear magnetic resonance studies of aluminophosphate molecular sieves. Journal of Physical Chemistry, 88, 6135-6139.

Bleam, W.F., Pfeffer, P.E., and Frye, J.S. (1989) ^{31}P solid-state nuclear magnetic resonance spectroscopy of aluminum phosphate minerals. Physics and Chemistry of Minerals, 16, 455-464.

Blount, A. (1974) The crystal structure of crandallite. American Mineralogist, 59, 41-47.

Boonchom, B., and Danvirutai, C. (2009) Kinetics and thermodynamics of thermal decomposition of synthetic $AlPO_4 \cdot 2H_2O$. Journal of Thermal Analysis and Calorimetry, 98, 771-777.

Bordat, P., Kirstein, J., Labéguerie, P., Merawa, M., and Brown, R. (2007) Structure and dynamics of $AlPO_4$-5 and other aluminophosphates: Classical molecular dynamics and ab initio calculations. Journal of Physical Chemistry C, 111, 10972-10981.

Brown, I.D. (2016) The chemical bond in inorganic chemistry. The bond valence model. 2nd Edition. Oxford University Press, U.K.

Calas, G., Galoisy, L., and Kiratisin, A. (2005) The origin of the green color of variscite. American Mineralogist, 90, 984-990.

Cheary, R.W. and Coelho, A.A. (1992) A Fundamental parameters approach of X-ray line-profile fitting. Journal of Applied Crystallography, 25, 109-121.

Cheary, R.W., Coelho, A.A., and Cline, J.P. (2004) Fundamental parameters line profile fitting in laboratory diffractometers. Journal of Research of the National Institute of Standard and Technology, 109, 1-25.

Coelho, A.A. (2003) Indexing of powder diffraction patterns by iterative use of singular value decomposition. Journal of Applied Crystallography, 36, 86-95.

Coelho, A.A. (2007) A charge-flipping algorithm incorporating the tangent formula for solving difficult structures. Acta Crystallographica A, 63, 400-406.

Dawson, D.M., Griffin, J.M., Seymour, V.R., Wheatley, P.S., Amri, M., Kurkiewicz, T., Guillou, N., Wimperis, S., Walton, R.I., and Ashbrook, S.E. (2017) A multinuclear NMR study of six forms of AlPO-34: Structure and motional broadening. Journal of Physical Chemistry C, 121, 1781-1793.

Delevoye, L., Fernandez, C., Morais, C.M., Amoureux, J.P., Montouillout, V., and Rocha, J. (2002) Double-resonance decoupling for resolution enhancement of ^{31}P solid-state MAS and $^{27}Al \rightarrow {}^{31}P$ MQHETCOR NMR. Solid State Nuclear Magnetic Resonance, 22, 501-512.

Drüppel, K., Hösch, A., and Franz, G. (2007) The system Al_2O_3-P_2O_5-H_2O at temperatures below 200 °C: Experimental data on the stability of variscite and metavariscite $AlPO_4 \cdot 2H_2O$. American Mineralogist, 92, 1695-1703.

Engelhardt, G., and Veeman, W. (1993) Assignment of the ^{27}Al and ^{31}P NMR spectra of the aluminophosphate molecular sieve VPI-5. Journal of the Chemical Society Chemical Communications, 622-623.

Flörke, O.W. (1967) Kristallisation und polymorphie von $AlPO_4$ und $AlPO_4$-SiO_2 mischkristallen. Zeitschrift für Kristallographie, 125, 134-136.

Ghose, S., and Tsang, T. (1973) Structural dependence of quadrupole coupling constant e^2qQ/h for ^{27}Al and crystal field parameter D for Fe^{3+} in aluminosilicates. American Mineralogist, 58, 748-755.

Gualtieri, A. (2000) Accuracy of XRPD QPA using the combined Rietveld-RIR method. Journal of Applied Crystallography, 33, 267-278.

Guinier, A., Bokij, G.B., Boll-Dornberger, K., Cowley, J.M., Ďurovič, S., Jagodzinski, H., Krishna, P., De Wolff, P.M., Zvyagin, B.B., Cox, D.E. and Goodman, P. (1984) Nomenclature of polytype structures. Report of the International Union of Crystallography Ad hoc Committee on the nomenclature of disordered, modulated and polytype structures. Acta Crystallographica A, 40, 399-404.

Guthrie Jr, G.D., Bish, D.L., and Reynolds Jr, R.C. (1995) Modeling the X-ray diffraction pattern of opal-CT. American Mineralogist, 80, 869-872.

Hawthorne, F.C. (2015) Toward theoretical mineralogy: a bond-topological approach. American Mineralogist, 100, 696-713.

Hensel, N., Franz, G., Gottschalk, M., Riedl, M., Wunder, B., Galbert, F., and Nissen, J. (2007) Polymorphism and solid solution in the system SiO_2-$AlPO_4$(-H_2O): a review and new synthesis experiments up to 3.5 GPa and 1573 K. Neues Jahrbuch für Mineralogie, 184, 131-149.

Ilyushin, G.D., and Blatov, V.A. (2017) Symmetry and topology code of the cluster self-assembly of framework MT structures of alumophosphates $AlPO_4(H_2O)_2$ (metavariscite and variscite) and $Al_2(PO_4)_2(H_2O)_3$ (APC). Crystallography Reports, 62, 174-184.

Kanehashi, K., Nemoto, T., and Saito, K. (2007) Through-bond and through-space connectivities of amorphous aluminophosphate by two-dimensional ^{27}Al–^{31}P heteronuclear NMR. Journal of Non-Crystalline Solids, 353, 4227-4231.

Kniep, R. (1986) Orthophosphates in the ternary system Al_2O_3-P_2O_5-H_2O. Angewandte Chemie, 25, 525-534.

Kniep, R., and Mootz, D. (1973) Metavariscite – A redetermination of its crystal structure. Acta Crystallographica B, 29, 2292-2294.

Kniep, R., Mootz, D., and Vegas, A. (1977) Variscite. Acta Crystallographica B, 33, 263-265.

Kolitsch, U., Weil, M., Kovrugin, V.M., and Krivovichev, S.V. (2020) Crystal chemistry of the variscite and metavariscite groups: Crystal structures of synthetic $CrAsO_4$ $2H_2O$, $TlPO_4$ $2H_2O$, $MnSeO_4$ $2H_2O$, $CdSeO_4$ $2H_2O$ and natural bonacinaite, $ScAsO_4$ $2H_2O$. Mineralogical Magazine, 84, 568-583.

Krivovichev, S.V. (2007) Crystal chemistry of selenates with mineral-like structures. IV. Crystal structure of $Zn(SeO_4)(H_2O)_2$, a new ,compound with a mixed framework of the variscite type. Geology of Ore Deposits, 49, 542-546.

Lagno, F., and Demopoulos, G.P. (2005) Synthesis of hydrated aluminum phosphate, $AlPO_4 \cdot 1.5H_2O$ ($AlPO_4$-H3), by controlled reactive crystallization in sulfate media. Industrial & Engineering Chemistry Research, 44, 8033-8038.

Larsen, III, E.S. (1942) The mineralogy and paragenesis of the variscite nodules from near Fairfield, Utah. American Mineralogist, 27, 281-300.

Lippmaa, E., Samoson, A., and Magi, M. (1986) High-resolution ^{27}Al NMR of aluminosilicates. Journal of the American Chemical Society, 108, 1730-1735.

Makovicky, E. (2006) Vaterite: Interpretation in terms of OD theory and its next of kin. American Mineralogist, 101, 1636-1641.

Marquardt, D. W. (1963) An algorithm for least-squares estimation of nonlinear parameters. Journal of the Society for Industrial and Applied Mathematics, 11, 431-331.

Momma, K., and Izumi, F. (2011) VESTA 3 for three-dimensional visualization of crystal, volumetric and morphology data. Journal of Applied Crystallography, 44, 1272-1276.

Müller, D., Jahn, E., Ladwig, G., and Haubenreisser, U. (1984) High-resolution solid-state ^{27}Al and ^{31}P NMR: correlation between chemical shift and mean Al-O-P Angle in $AlPO_4$ polymorphs. Chemical Physics Letters, 109, 332-336.

Muraoka, Y., and Kihara, K. (1997) The temperature dependence of the crystal structure of berlinite, a quartz-type form of $AlPO_4$. Physics and Chemistry of Minerals, 24, 243-253.

Ng, H.N., and Calvo, C. (1976) X-ray study of the α-β transformation of berlinite ($AlPO_4$). Canadian Journal of Physics, 54, 638-647.

Oelkers, E. H., and Valsami-Jones, E. (2008) Phosphate mineral reactivity and global sustainability. Elements, 4, 83-87.

Oszlányi, G., and Sütő, A (2004) Ab initio structure solution by charge flipping. Acta Crystallographica A, 60, 134-141.

Palatinus, L. (2013) The charge-flipping algorithm in crystallography. Acta Crystallographica B, 69, 1-16.

Pawley, G. S. (1981) Unit-cell refinement from powder diffraction scans. Journal of Applied Crystallography, 14, 357-361.

Pawlowski, S. (1965) Bond properties of aluminum phosphates from the point of refractory ceramics. Epitoanyag, 17, 333-337.

Prado-Herrero, P., Garcia-Guinea, J., Crespo-Feo, E., and Correcher, V. (2010) Temperature-induced transformation of metavariscite to berlinite. Phase Transitions, 83, 440-449.

Price, G. D., and Yeomans, J. (1984) The application of the ANNNO model to polytypic behaviour. Acta Crystallographica B, 40, 448-453.

Rietveld, H.M. (1967) Line profiles of neutron powder-diffraction peaks for structure refinement. Acta Crystallographica, 22, 151-152.

Rietveld, H.M. (1969) A profile refinement method for nuclear and magnetic structures. Journal of Applied Crystallography, 2, 65-71.

Robinson, K., Gibbs, G.V., and Ribbe, P.H. (1971) Quadratic elongation: a quantitative measure of distortion in coordination polyhedra. Science, 172, 567-570.

Rothon, R. N. (1981) Solution deposited metal phosphate coatings. Thin Solid Films, 77, 149-153.

Salvador, P.S., and Fayos, J. (1972) Some aspects of the structural relationship between "Messbach-type" and "Lucin-type" variscites. American Mineralogist, 57, 36-44.

Samoson, A. (1985) Satellite transition high-resolution NMR of quadrupolar nuclei in powders. Chemical Physics Letters, 119, 29-32.

Smith, J., Yeomans, J., and Heine, V. (1984). A new theory of polytypism. In T. Tsakalakos, ed., Modulated Structure Materials, 95-105. Springer, Dordrecht.

Smith, J.V. (1977) Enumeration of 4-connected 3-dimensional nets and classification of framework silicates. I. Perpendicular linkage from simple hexagonal net. American Mineralogist, 62, 703-709.

Taxer, K. and Bartl, H. (2004) On the dimorphy between the variscite and clinovariscite group: refined fine structural relationship of strengite and clinostrengite, $Fe(PO_4)\cdot 2H_2O$. Crystal Research and Technology, 39, 1080-1088.

Wilson, S. T., Lok, B. M., Messina, C. A., Cannan, T. R., and Flanigen, E. M. (1982) Aluminophosphate molecular sieves: A new class of microporous crystalline inorganic solids. Journal of the American Chemical Society, 104, 1146-1147.

Wise, W.S., and Loh, S.E. (1976) Equilibria and origin of minerals in the system Al_2O_3-$AlPO_4$-H_2O. American Mineralogist, 61, 409-413.

d'Yvoire, F.B. (1961) Étude des phosphates d'aluminium et de fer trivalent. I. L'orthophosphate neutre d´aluminium. Bulletin de la Société Chimique de France, 372, 1762-1776.

Zvyagin, B.B. (1988) Polytypism of crystal structures. Computers & Mathematics with Applications, 16, 569-591.

LIST OF FIGURE CAPTIONS

~~**Figure 1.** Graphical output of the structure solution of variscite*2O* at RT obtained by the CFA as implemented in TOPAS v.5.0, showing oxygen atoms in red, phosphate tetrahedra in gold, and Al octahedra in gray.~~

Figure 1. Rietveld refinement plot for the variscite sample collected at RT. Variscite*2O*, metavariscite, crandallite, and quartz have phase fractions of ~86%, 7%, 4%, and 3%, respectively. The experimental pattern is represented by black dots, phases contributing to the best-fit refinement profile are the red, blue, purple, and green continuous lines for the variscite*2O*, metavariscite, crandallite, and quartz phases, respectively, and the lower gray curve is the difference between calculated and observed intensities.

Figure 2. (*a*) Sequence of XRD patterns for the variscite sample collected at HT; and (*b*) comparison of the variscite XRD data measured at RT before (gray line) and after (black line) thermal treatment. The presence of metavariscite (up to 323 K) and quartz (throughout the investigated temperature range) is highlighted with small arrows and a cross, respectively.

Figure 3. Schematic representation of the $AlPO_4$-var*2O* polyhedral arrangement in a perspective view along the *c*-axis, where isolated PO_4 tetrahedra share corners with isolated AlO_4 tetrahedra. Bridging oxygen atoms are red spheres. Figure obtained using the VESTA v.3.4.5 visualizer (Momma and Izumi 2011).

Figure 4. Rietveld refinement plot of the powder diffraction pattern for the variscite sample collected at RT after heating at 723 K. $AlPO_4$-var*2O*, crandallite and quartz have phase fractions of ~94%, 2%, and 4%, respectively. The experimental pattern is represented by black dots, phases contributing to the best-fit refinement profile are the red, purple, and green continuous lines for $AlPO_4$-var*2O*, crandallite and quartz, respectively, and the lower gray curve is the difference between calculated and observed intensities.

Figure 5. Simultaneous TG (black line) and DTA (gray line) curves for the variscite sample heated in air from 297 to 773 K at a rate of 10 K min^{-1}. DTA endotherms (downward inflections in the DTA curve) were observed between 325 and 355 K and at 425 K. Horizontal dashed lines represent the theoretical dehydration values of 0.5, 1, 1.5, and 2 molecules of H_2O, respectively, for a compound with formula $AlPO_4 \cdot 2H_2O$.

Figure 6. ^{31}P (left panel, (*a*) and (*b*)) and ^{27}Al (right panel) MAS/NMR spectra of variscite*2O* (top) and after heating at 523 K (bottom). Insets in (*c*) show ±1 satellite spinning sidebands, clearly resolving signals from Al1 and Al2.

Figure 7. Sheared and scaled ^{27}Al MQ-MAS NMR spectrum of variscite*2O* (left panel) with summed projections plotted at top and right. (right panel) F2 cross-sections taken at the isotropic F1 peak positions -6.8 ppm (top) and -1.8 ppm (bottom), showing second-order quadrupolar anisotropic peak shapes.

Figure 8. Schematic representation of the variscite*2O* ~~(*a*) and variscite*1O* (*b*)~~ polyhedral arrangement~~s~~ in a perspective view. Isolated PO_4 tetrahedra share corners with isolated $AlO_4(OH_2)_2$ octahedra. Bridging and terminal (i.e., H_2O molecules) oxygen atoms are red and blue spheres, respectively. Figure obtained using the VESTA v.3.4.5 visualizer (Momma and Izumi 2011).

Figure 9. Horizontal 3-connected net in a perspective view (*a* and *c*), and in the conventional 2D representation (further details in Smith 1977) along the [001] direction (*b* and *d*), for variscite*1O* (*a* and *b*) and *2O* (*c* and *d*). The unit cell is marked by dashed lines. Black dots and white circles show opposite directions of vertical linkage (upward and downward, respectively). Hexagons in (*a*) and (*c*) show the sequence created by adjacent nodes.

Figure 10. 2D representation of nets based on hexagons for variscite*1O* and *2O* (*a* and *b*), where black and white vertices denote tetrahedra and octahedra, respectively. ~~A schematic representation of the linkage of adjacent 2D hexagonal nets to a 3D topological graph is provided for variscite*1O* and *2O* (*b* and *d*), where gray squares highlight the location of the four-membered rings.~~

Figure 11. Graphical representation of the variscite*1O* (*a*) and *2O* (*b*) topology. Boat-shaped eight-membered rings and six-membered rings are in blue and red, respectively, and gray squares highlight the location of the four-membered rings.

Figure 12. Temperature dependence of the unit-cell volume (*a*); and normalized unit-cell parameters (*b*) for the $AlPO_4$-var*2O* phase after complete dehydration of variscite*2O* in the investigated sample. Dashed lines are a reader's guide. Data at 298.15 K refer to XRPD data

measured at RT after heating treatment at 723 K. Symbol sizes exceed the estimated uncertainties in measurements.

This is the peer-reviewed, final accepted version for American Mineralogist, published by the Mineralogical Society of America.
The published version is subject to change. Cite as Authors (Year) Title. American Mineralogist, in press.
DOI: https://doi.org/10.2138/am-2022-8119. http://www.minsocam.org/

TABLES

Table 1. Rietveld refinement agreement factors, quantitative phase analysis, and unit-cell parameters for phases in the variscite sample collected at RT. ~~Note: δ is the calculated crystal density.~~

Refinement agreement factors							
R_{exp} = 0.031		R_{wp} = 0.076	R_p = 0.057		G.O.F. = 0.025		
Quantitative phase analysis & unit-cell parameters							
Phase	Wt %	s.g.	*a*(Å)	*b*(Å)	*c*(Å)	β(°)	*V*(Å^3)
variscite*2O*	86.4(1)	*Pbca*	9.8980(2)	17.1820(3)	9.6617(2)	–	1643.14(5)
metavariscite	7.1(1)	$P2_1/n$	5.1802(5)	9.5342(11)	8.4526(6)	90.43(1)	417.45(7)
crandallite	3.5(1)	*R*-3*m*	7.0112(14)	–	16.134(6)	–	686.8(4)
quartz	3.0(1)	$P3_121$	4.9160(2)	–	5.4084(4)	–	113.19(1)

Table 2. Selected metal-oxygen bond distances and bond angles with their standard deviations for the variscite*2O* crystal structure at RT.

$AlPO_4{\cdot}2H_2O$ (s.g. *Pbca* (61); Z = 8)							
Intrapolyhedral metal-oxygen bond distances (Å)							
Al1–O11	1.928(5)	Al2–O12	1.919(5)	P1–O11	1.535(5)	P2–O21	1.530(5)
Al1–O14	1.906(6)	Al2–O13	1.920(6)	P1–O12	1.536(6)	P2–O22	1.532(6)
Al1–O22	1.896(6)	Al2–O21	1.898(6)	P1–O13	1.546(6)	P2–O23	1.531(5)
Al1–O24	1.903(6)	Al2–O23	1.904(5)	P1–O14	1.529(5)	P2–O24	1.539(6)
Al1–O_W11	1.925(6)	Al2–O_W21	1.928(6)	⟨P1–O⟩	1.537(7)	⟨P2–O⟩	1.533(6)
Al1–O_W12	1.921(6)	Al2–O_W22	1.943(6)	TQE ($P1O_4$)	1.002	TQE ($P2O_4$)	1.005
⟨Al1–O⟩	1.913(6)	⟨Al2–O⟩	1.919(6)				
OQE($Al1O_4(OH_2)_2$)	1.003	OQE($Al2O_4(OH_2)_2$)	1.004				
Intrapolyhedral bond angles (°)							
O11–Al1–O14	175.0(3)	O12–Al2–O13	92.0(3)	O11–P1–O12	113.2(4)	O21–P2–O22	104.7(4)
O11–Al1–O22	91.9(3)	O12–Al2–O21	85.9(3)	O11–P1–O13	110.6(3)	O21–P2–O23	105.2(4)
O11–Al1–O24	91.5(3)	O12–Al2–O23	92.7(3)	O11–P1–O14	108.1(4)	O21–P2–O24	113.1(4)
O11–Al1–O_W11	88.6(3)	O12–Al2–O_W21	177.3(3)	O12–P1–O13	105.6(4)	O22–P2–O23	115.3(4)
O11–Al1–O_W12	90.4(3)	O12–Al2–O_W22	91.1(3)	O12–P1–O14	109.9(3)	O22–P2–O24	110.7(4)
O14–Al1–O22	93.0(3)	O13–Al2–O21	87.7(3)	O13–P1–O14	109.4(4)	O23–P2–O24	107.8(3)
O14–Al1–O24	90.1(3)	O13–Al2–O23	93.1(3)	⟨O–P1–O⟩	109.5(4)	⟨O–P2–O⟩	109.5(4)
O14–Al1–O_W11	86.6(3)	O13–Al2–O_W21	89.9(3)	TAV ($P1O_4$)	6.33	TAV ($P2O_4$)	18.50
O14–Al1–O_W12	88.0(3)	O13–Al2–O_W22	172.9(3)				
O22–Al1–O24	84.4(3)	O21–Al2–O23	178.5(3)				
O22–Al1–O_W11	174.7(3)	O21–Al2–O_W21	96.0(3)				
O22–Al1–O_W12	96.9(3)	O21–Al2–O_W22	86.1(3)				
O24–Al1–O_W11	90.3(3)	O23–Al2–O_W21	85.3(3)				
O24–Al1–O_W12	177.7(3)	O23–Al2–O_W22	93.2(3)				
O_W11–Al1–O_W12	88.4(3)	O_W21–Al2–O_W22	87.2(3)				
⟨O–Al1–O⟩	107.2(3)	⟨O–Al2–O⟩	107.3(3)				
OAV ($Al1O_4(OH_2)_2$)	10.41	OAV($Al2O_4(OH_2)_2$)	12.25				
Interpolyhedral bond angles (°)							
Al1–O11–P1	137.1(4)	Al2–O12–P1	138.0(4)	Al1-O22-P2	138.5(4)	Al2-O21-P2	133.3(4)
Al1–O14–P1	143.5(4)	Al2–O13–P1	141.8(4)	Al1-O24-P2	144.6(4)	Al2-O23-P2	138.1(4)
⟨Al1–O–P1⟩	140.3(4)	⟨Al2–O–P1⟩	139.9(4)	⟨Al1–O–P2⟩	141.6(4)	⟨Al2–O–P2⟩	135.7(4)

TQE = Tetrahedral Quadratic Elongation; TAV = Tetrahedral Angle Variance (°^{2});
OQE = Octahedral Quadratic Elongation; OAV = Octahedral Angle Variance (°^{2}); (Robinson et al. 1971).

This is the peer-reviewed, final accepted version for American Mineralogist, published by the Mineralogical Society of America.
The published version is subject to change. Cite as Authors (Year) Title. American Mineralogist, in press.
DOI: https://doi.org/10.2138/am-2022-8119. http://www.minsocam.org/

Table 3. Rietveld refinement agreement factors, quantitative phase analysis, and unit-cell parameters for the variscite sample measured at RT after heating at 723 K. ~~Note: δ is the calculated crystal density.~~

Refinement agreement factors						
R_{exp} = 0.049		R_{wp} = 0.102	R_p = 0.075		G.O.F. = 0.021	
Quantitative phase analysis & unit-cell parameters						
Phase	Wt %	s.g.	*a*(Å)	*b*(Å)	*c*(Å)	*V*(Å^3)
$AlPO_4$-var*2O*	94.4(2)	*Pbca*	9.9703(9)	17.1523(15)	8.6314(7)	1476.1(2)
crandallite	1.8(2)	*R*-3*m*	6.942(5)	–	15.920(23)	664.6(1.4)
quartz	3.8(1)	$P3_121$	4.9163(5)	–	5.4049(9)	113.13(3)

Table 4. Selected metal-oxygen bond distances and bond angles with standard deviations for the $AlPO_4$-var*2O* crystal structure.

$AlPO_4$-var*2O* (s.g. *Pbca* (61); Z = 8)							
Intrapolyhedral metal-oxygen bond distances (Å)							
Al1–O11	1.679(7)	Al2–O12	1.733(8)	P1–O11	1.531(6)	P2–O21	1.553(8)
Al1–O14	1.717(8)	Al2–O13	1.699(8)	P1–O12	1.535(8)	P2–O22	1.547(8)
Al1–O22	1.712(7)	Al2–O21	1.705(9)	P1–O13	1.529(7)	P2–O23	1.541(7)
Al1–O24	1.702(8)	Al2–O23	1.701(8)	P1–O14	1.557(7)	P2–O24	1.533(7)
⟨Al1–O⟩	1.703(7)	⟨Al2–O⟩	1.710(8)	⟨P1–O⟩	1.538(7)	⟨P2–O⟩	1.543(7)
TQE ($Al1O_4$)	1.004	TQE ($Al2O_4$)	1.003	TQE ($P1O_4$)	1.001	TQE ($P2O_4$)	1.008
Intrapolyhedral bond angles (°)							
O11–Al1–O14	109.1(5)	O12–Al2–O13	110.2(5)	O11–P1–O12	107.8(5)	O21–P2–O22	100.8(5)
O11–Al1–O22	116.6(4)	O12–Al2–O21	108.9(4)	O11–P1–O13	109.6(5)	O21–P2–O23	109.6(6)
O11–Al1–O24	109.5(4)	O12–Al2–O23	104.1(4)	O11–P1–O14	108.6(5)	O21–P2–O24	111.2(5)
O14–Al1–O22	109.7(4)	O13–Al2–O21	114.8(5)	O12–P1–O13	108.0(4)	O22–P2–O23	116.4(5)
O14–Al1–O24	105.3(4)	O13–Al2–O23	107.9(4)	O12–P1–O14	110.1(5)	O22–P2–O24	104.9(5)
O22–Al1–O24	106.1(4)	O21–Al2–O23	110.4(5)	O13–P1–O14	112.6(5)	O23–P2–O24	113.2(5)
⟨O–Al1–O⟩	109.4(4)	⟨O–Al2–O⟩	109.4(4)	⟨O–P1–O⟩	109.5(5)	⟨O–P2–O⟩	109.4(5)
TAV ($Al1O_4$)	15.99	TAV($Al2O_4$)	12.19	TAV ($P1O_4$)	3.21	TAV($P2O_4$)	32.23
Interpolyhedral bond angles (°)							
Al1–O11–P1	153.2(6)	Al2–O12–P1	154.8(5)	Al1-O22-P2	146.9(5)	Al2-O21-P2	144.7(6)
Al1–O14–P1	140.3(5)	Al2–O13–P1	142.9(5)	Al1-O24-P2	144.0(6)	Al2-O23-P2	156.5(5)
⟨Al1–O–P1⟩	146.8(6)	⟨Al2–O–P1⟩	148.9(5)	⟨Al1–O–P2⟩	145.5(5)	⟨Al2–O–P2⟩	150.6(5)

TQE = Tetrahedral Quadratic Elongation; TAV = Tetrahedral Angle Variance (°^{2}); (Robinson et al. 1971).

This is the peer-reviewed, final accepted version for American Mineralogist, published by the Mineralogical Society of America.
The published version is subject to change. Cite as Authors (Year) Title. American Mineralogist, in press.
DOI: https://doi.org/10.2138/am-2022-8119. http://www.minsocam.org/

Table 5. NMR parameters derived from ^{31}P and ^{27}Al NMR spectra of variscite*2O* and of $AlPO_4$-var*2O* obtained from variscite*2O* by heating in air at 523 K for 4h. All NMR data were acquired at RT. Values in parentheses represent estimated uncertainty in the last digits. Note that signals were not resolved for crystallographically distinct P and Al sites for $AlPO_4$-var*2O*.
n.d. denotes parameters not determined.

sample		δ_{iso} (ppm)	*FWHM* (ppm)	calculated δ_{iso} (ppm)[1]	C_q (MHz)	η
variscite*2O*						
	P1	-20.3(1)	0.9	-20.1 to -20.3		
	P2	-17.0(1)	0.8	-18.6 to -18.2		
	Al1	-8.9(2)			2.7(1)	0.5(1)
	Al2	-6.5(2)			3.5(1)	0.95(5)
$AlPO_4$-var*2O*						
	P1	-28.7(1)	2.8	-29.3 to -29.7		
	P2			-29.4 to -30.0		
	Al1,Al2	40.2(1)	4.0		2.0(2)	*n.d.*

[1]range of values from expressions given by Kanehashi et al. (2007) and Dawson et al. (2017)

Table 6. BV calculation (in v.u.; Hawthorne 2015; Brown 2016) for Al and P polyhedra in variscite*2O* and $AlPO_4$-var*2O*.

variscite*2O*	Al1	O11	-0.47	Al2	O12	-0.48	P1	O11	-1.25	P2	O21	-1.27
		O14	-0.50		O13	-0.48		O12	-1.25		O22	-1.26
		O22	-0.52		O21	-0.51		O13	-1.21		O23	-1.26
		O24	-0.51		O23	-0.51		O14	-1.27		O24	-1.23
		O_W11	-0.48		O_W21	-0.47						
		O_W12	-0.48		O_W22	-0.45						
	BV_{sum}		*2.96*			*2.91*			*4.98*			*5.02*
$AlPO_4$-var*2O*	Al1	O11	-0.93	Al2	O12	-0.80	P1	O11	-1.26	P2	O21	-1.19
		O14	-0.84		O13	-0.88		O12	-1.25		O22	-1.21
		O22	-0.85		O21	-0.86		O13	-1.27		O23	-1.23
		O24	-0.87		O23	-0.87		O14	-1.18		O24	-1.26
	BV_{sum}		*3.48*			*3.42*			*4.96*			*4.88*

This is the peer-reviewed, final accepted version for American Mineralogist, published by the Mineralogical Society of America.
The published version is subject to change. Cite as Authors (Year) Title. American Mineralogist, in press.
DOI: https://doi.org/10.2138/am-2022-8119. http://www.minsocam.org/

FIGURE 1

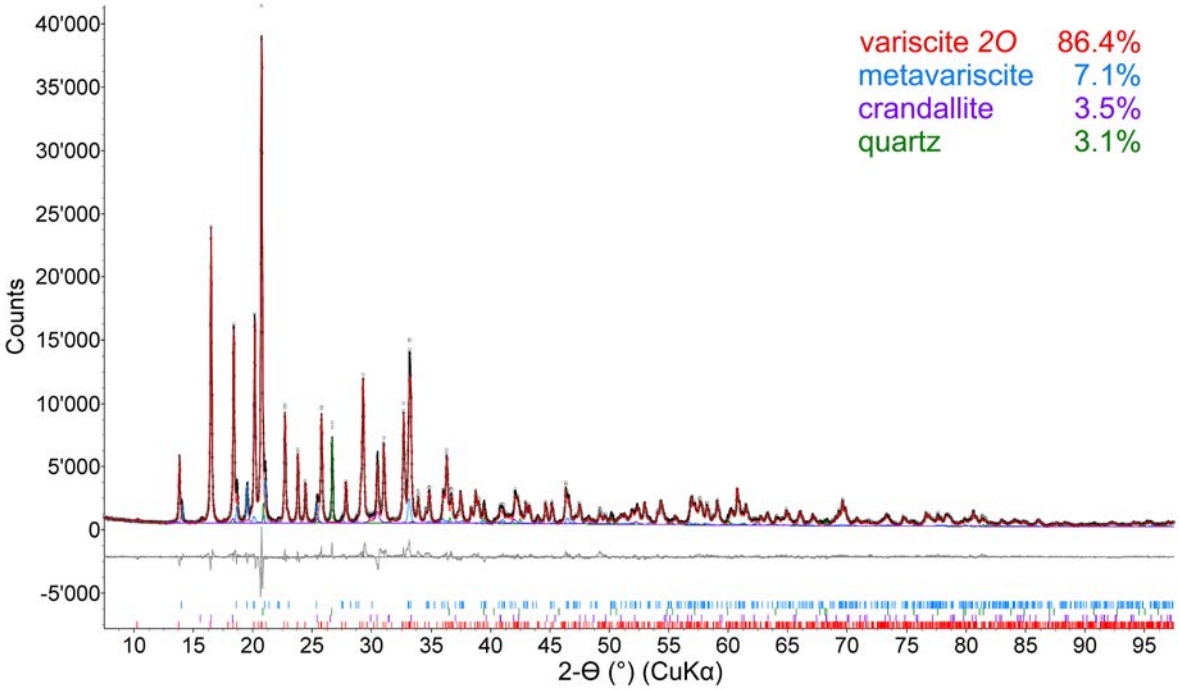

FIGURE 2 (a and b)

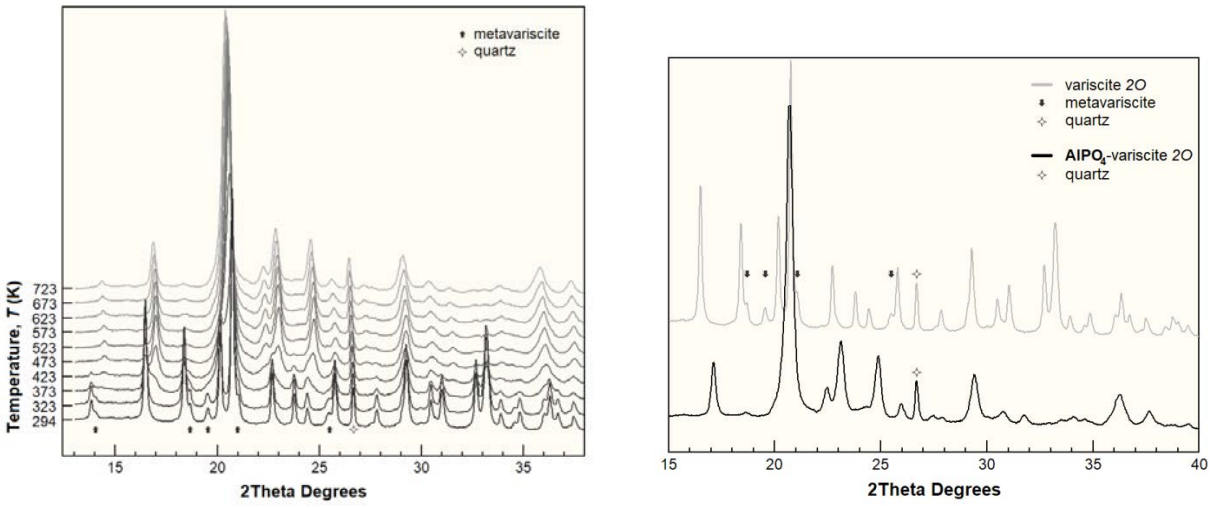

a *b*

This is the peer-reviewed, final accepted version for American Mineralogist, published by the Mineralogical Society of America.
The published version is subject to change. Cite as Authors (Year) Title. American Mineralogist, in press.
DOI: https://doi.org/10.2138/am-2022-8119. http://www.minsocam.org/

FIGURE 3

FIGURE 4

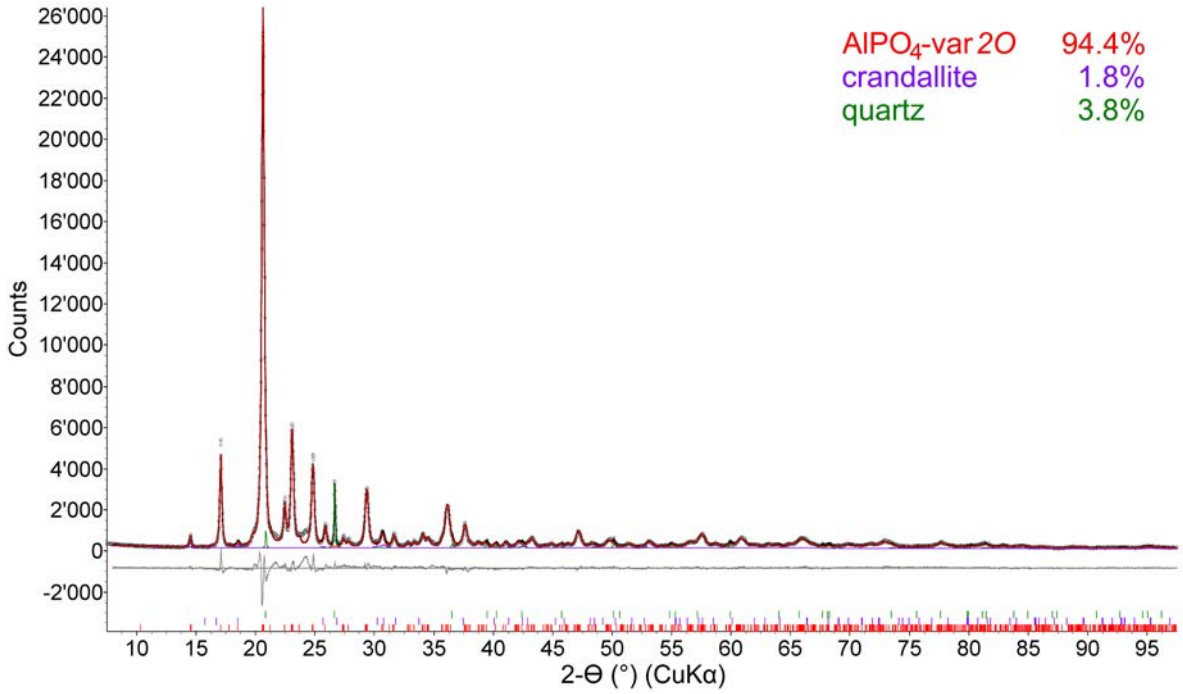

This is the peer-reviewed, final accepted version for American Mineralogist, published by the Mineralogical Society of America.
The published version is subject to change. Cite as Authors (Year) Title. American Mineralogist, in press.
DOI: https://doi.org/10.2138/am-2022-8119. http://www.minsocam.org/

FIGURE 5

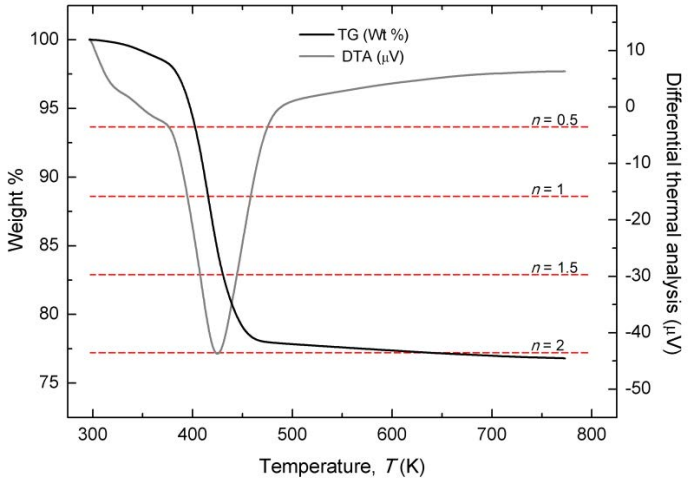

FIGURE 6

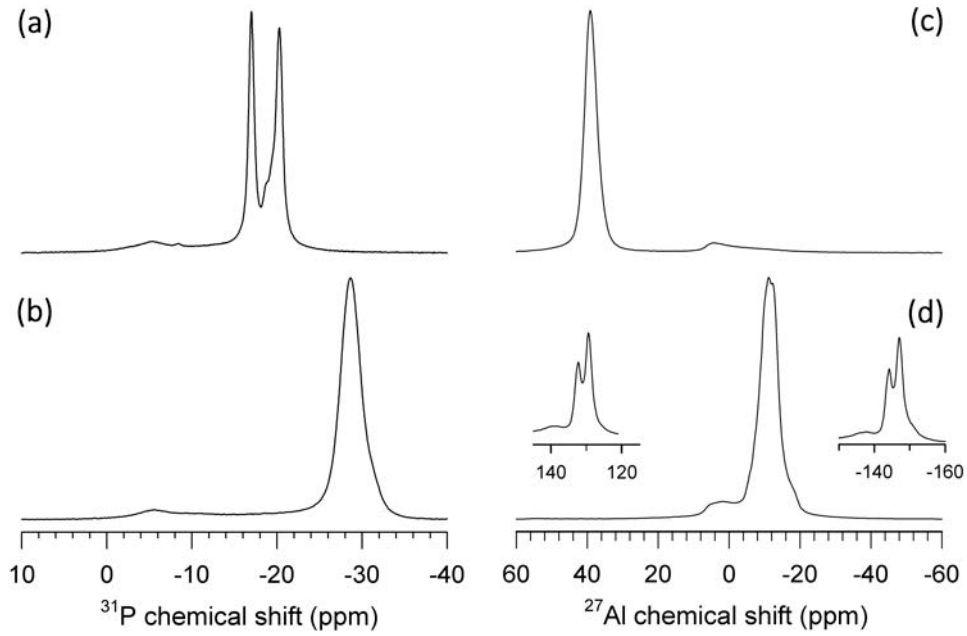

This is the peer-reviewed, final accepted version for American Mineralogist, published by the Mineralogical Society of America.
The published version is subject to change. Cite as Authors (Year) Title. American Mineralogist, in press.
DOI: https://doi.org/10.2138/am-2022-8119. http://www.minsocam.org/

FIGURE 7

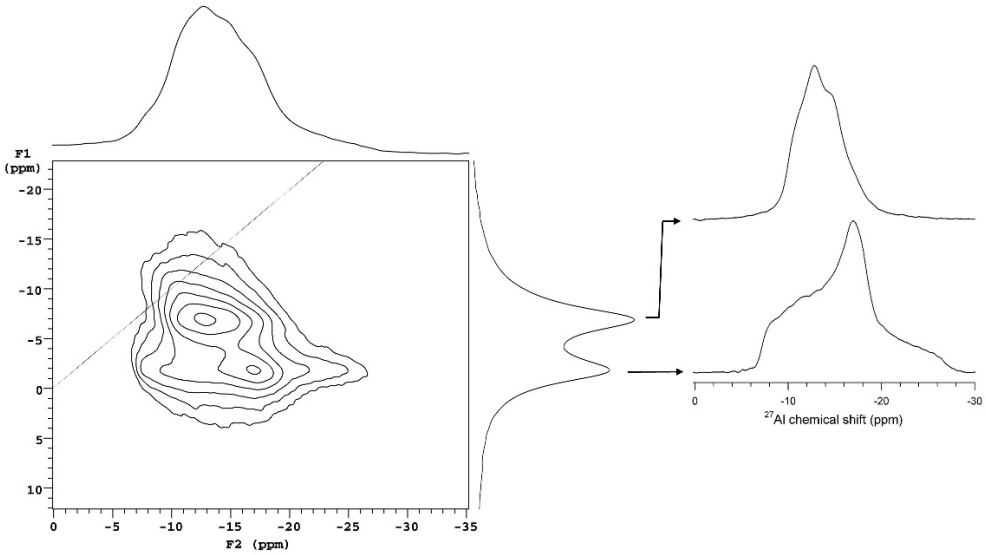

FIGURE 8 (a and b)

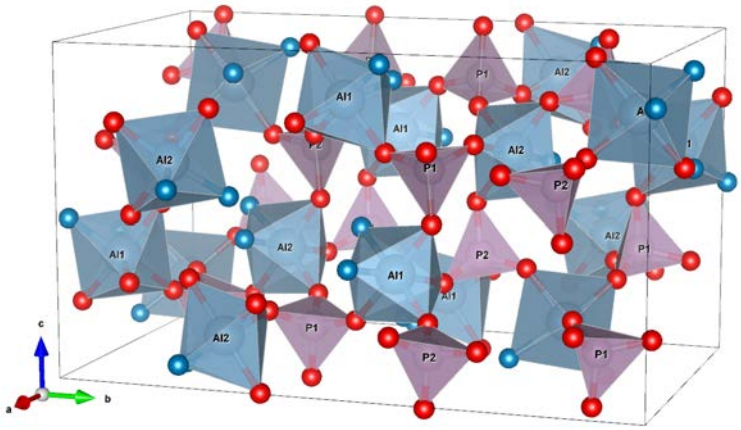

This is the peer-reviewed, final accepted version for American Mineralogist, published by the Mineralogical Society of America.
The published version is subject to change. Cite as Authors (Year) Title. American Mineralogist, in press.
DOI: https://doi.org/10.2138/am-2022-8119. http://www.minsocam.org/

FIGURE 9 (a-d)

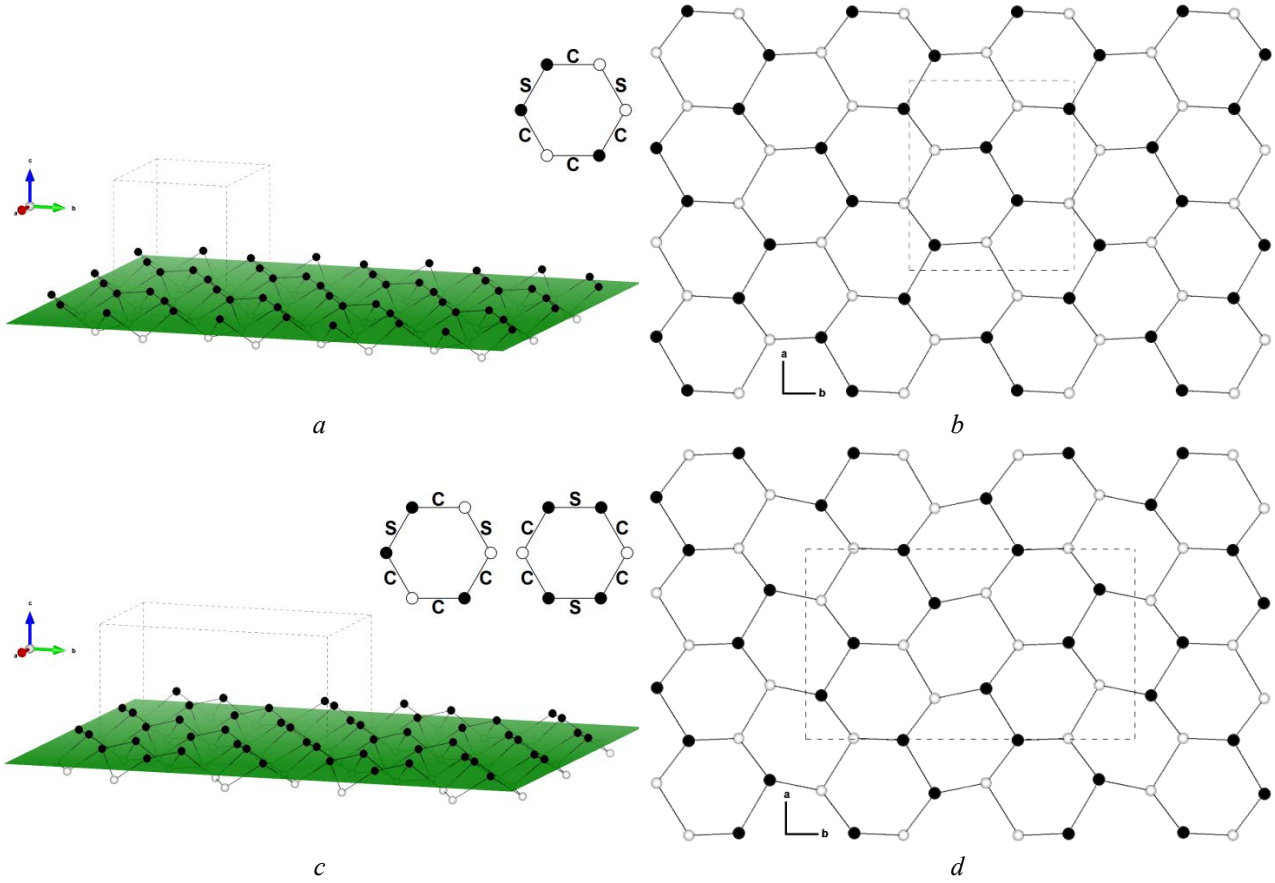

FIGURE 10 (*a* and *b*)

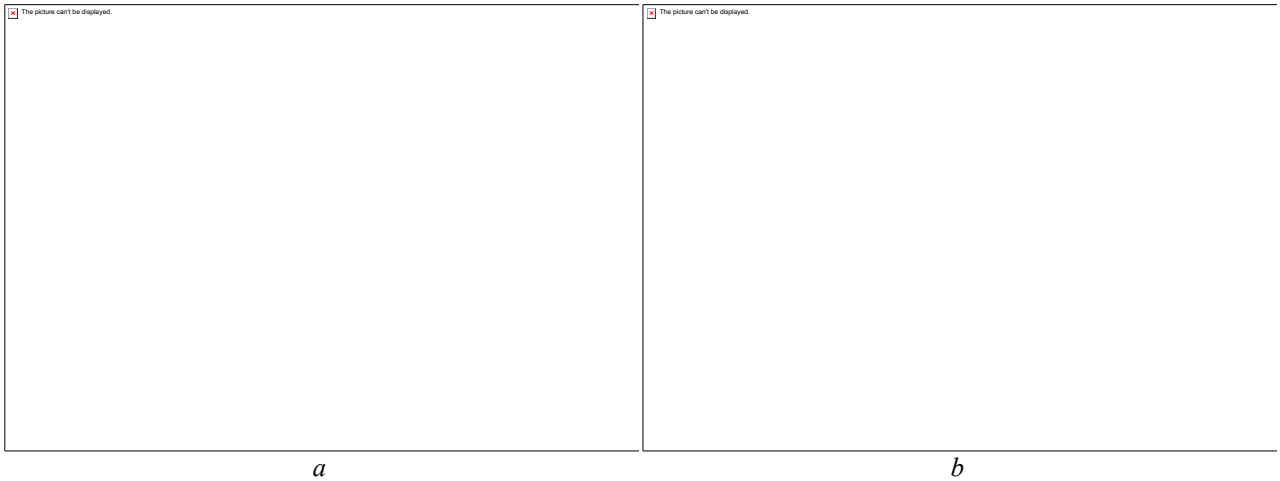

a *b*

This is the peer-reviewed, final accepted version for American Mineralogist, published by the Mineralogical Society of America.
The published version is subject to change. Cite as Authors (Year) Title. American Mineralogist, in press.
DOI: https://doi.org/10.2138/am-2022-8119. http://www.minsocam.org/

FIGURE 11 (*a* and *b*)

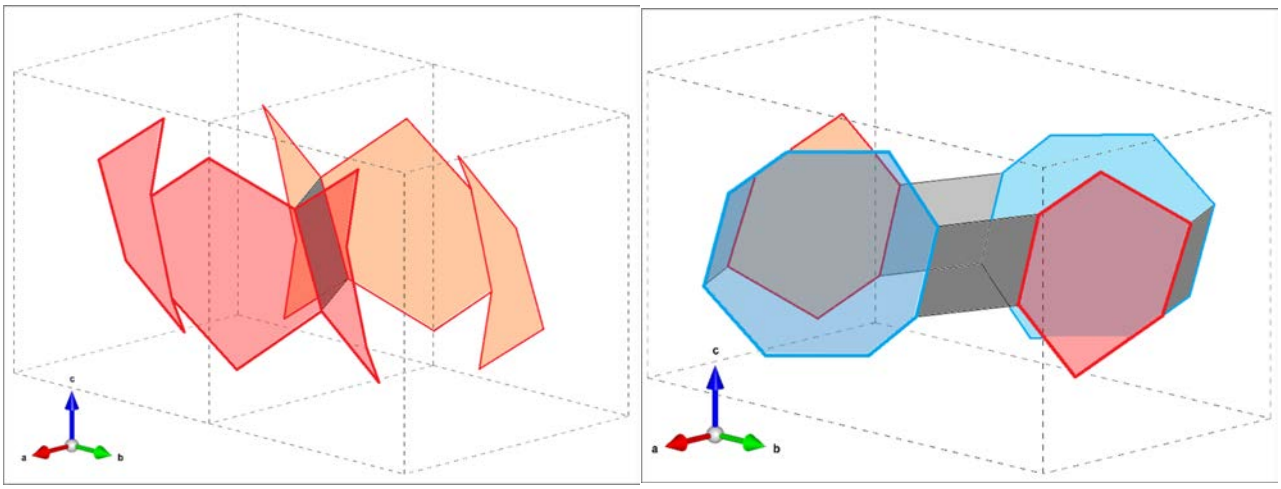

a *b*

FIGURE 12 (a and b)

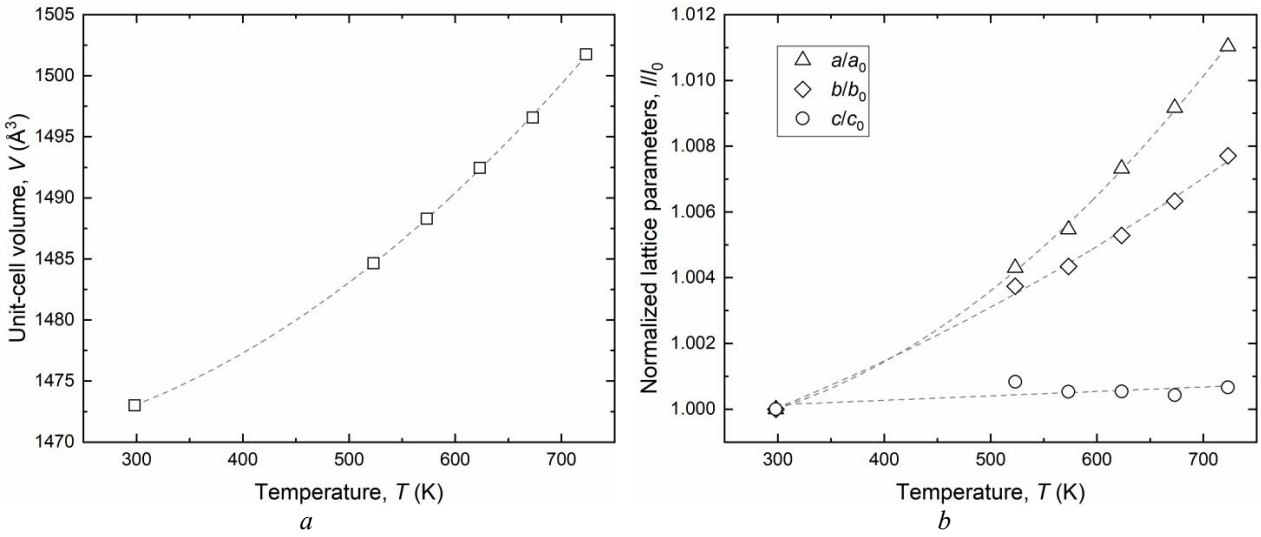

a *b*